ACS APPLIED MATERIALS & INTERFACES

Research Article

www.acsami.org

Engineering Hybrid between MnO and N-Doped Carbon to Achieve Exceptionally High Capacity for Lithium-Ion Battery Anode

Ying Xiao,[†] Xia Wang,[†] Wei Wang,[†] Di Zhao,[†] and Minhua Cao*[,†,‡]

[†]Key Laboratory of Cluster Science, Ministry of Education of China, Beijing Key Laboratory of Photoelectronic/Electrophotonic Conversion Materials, Department of Chemistry, Beijing Institute of Technology, Beijing 100081, P. R. China

[‡]State Key Laboratory of Chemical Resource Engineering, Beijing University of Chemical Technology, Beijing, 100029, P. R. China

Supporting Information

ABSTRACT: A facile and low-cost strategy is demonstrated for preparing MnO/C−N hybrid, in which the MnO nanoparticles chemically combine with N-doped C by Mn−N bonding to achieve the hybridization of MnO with N-doped C. When served as an anode in lithium ion batteries (LIBs), the resultant hybrid manifested high capacity, excellent cyclability, and superior rate capability. A lithium storage capacity of 1699 mAh g^{-1} could be obtained at 0.5 A g^{-1} after 170 discharge−charge cycles. Even at a current density up to 5 A g^{-1}, a high reversible capacity (907.8 mAh g^{-1}) can be retained after 400 cycles. The excellent lithium storage performance of the MnO/C−N hybrid can be ascribed to the synergetic effects of several factors including the unique hybrid structure, the N-doping and the chemical bonding of MnO and N-doped C.

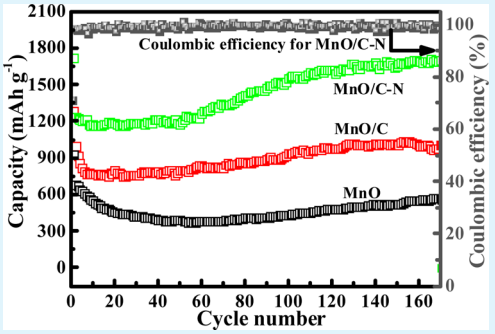

KEYWORDS: *manganese oxide, nitrogen-doped carbon, hybrid, electrochemistry, high capacity, lithium ion batteries*

1. INTRODUCTION

Lithium ion batteries (LIBs) have been attracted significant interest in the past decades, which are considered to be an important power source being applied in portable electronics and even in the field of electric vehicles.[1−4] However, many aspects such as energy density, cycling stability, and economic efficiency are still facing large challenges. In particular, searching for low-cost electrode materials with high energy density and cycling stability is one of the hottest topics in the research of LIBs.[5] 3d transition-metal oxides such as Mn_3O_4,[6] Co_3O_4,[7] NiO,[8] Fe_2O_3,[9] Fe_3O_4,[10] MoO_2,[11] have been intensively studies as potential high-performance electrodes for LIBs because of their high theoretical specific capacities, low cost and easy availability. Among various transition metal oxides, MnO-based materials are promising anodes for LIBs because of their low cost, low conversion potential and voltage hysteresis, high density, environmental benignity, and nature abundance.[12−15] Besides, MnO has a theoretical specific capacity (755 mAh g^{-1}), which is far larger than that of currently used graphite (372 mAh g^{-1}). Nevertheless, like other transition metal oxides, MnO-based materials also suffer from two typical problems, poor durability and low electrical conductivity, which greatly impede their application in LIBs.[14−16] The drastic volume change during Li^+ intercalation−decalation process between the lattices via the conversion reaction mechanism easily leads to the pulverization of the MnO electrode, which inevitably brings in rapid capacity fading with further cycling. On the other hand, the low electrical conductivity generally results in the inferior rate capability. Consequently, only if these two aspects are fully taken into consideration could the high performance of MnO-based electrodes be achieved.

Up to now, many strategies have been proposed to tackle the above-mentioned issues of MnO-based anodes. One of the effective approaches is to reduce the dimension of the electrode materials from micrometer to the nanometer regime. Generally speaking, nanomaterials can not only accommodate the strains of Li^+ insertion/desertion, but also shorten the transport path of Li ions and electrons, significantly improving the conductivity and discharge/charge rates when compared with the bulk ones.[5,17,18] Additionally, smaller particles will have larger surface area, which can facilitate the Li^+ exchange between the electrode and electrolyte. However, this strategy is relatively limited in improving the lithium storage performance of MnO. The other widely used method is doping N or hybridizing with conductive materials such as metal and carbon to increase the conductivity of the electrode materials.[4,13,15,16] This approach has been proved to be effective for enhancing the rate performance and cycling stability of the MnO electrode, compared with pristine ones, which demonstrates the potential advantages of MnO-based hybrid electrodes. For instance, Huang's group reported MnO/graphene hybrid, which exhibits exceptional capacity of 2014.1 mAh g^{-1} at 0.2 A g^{-1} after 150 cycles and 843.3 mAh g^{-1} after 400 cycles at 2 A g^{-1}, indicating its high effectiveness in improving the lithium storage capability of MnO.[16] Chen and his co-workers

Received: November 15, 2013
Accepted: January 10, 2014
Published: January 10, 2014

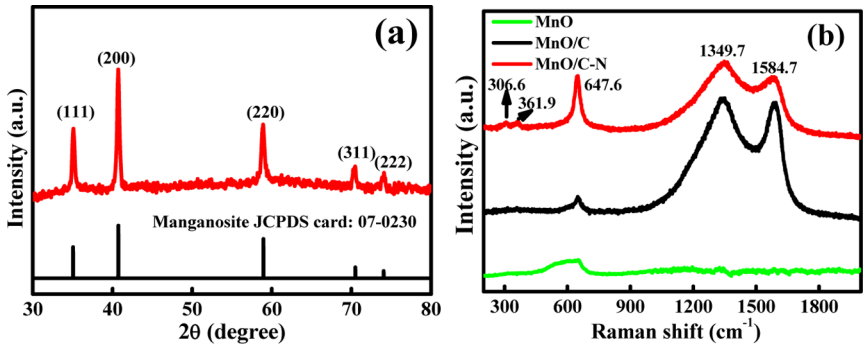

Figure 1. (a) XRD pattern of the MnO/C−N hybrid. (b) Raman spectra of the MnO/C−N hybrid, MnO/C, and MnO.

synthesized N-doped MnO/graphene nanosheets, which exhibits large reversible capacity of 772 mAh g^{-1} at 0.1 A g^{-1} after 90 cycles and 202 mAh g^{-1} at 5 A g^{-1}.[19] Moreover, carbon-encapsulated nano-MnO composite with novel multiple structure loaded on N-doped carbon webs was also prepared by using polypyrrole webs as both template and precursor. The resultant product delivered a capacity of 1268 mAh g^{-1} after 700 cycles at 1.0 A g^{-1}.[20] All the above-mentioned reports illustrated that the hybridization is significant efficient for the improvement of lithium storage performance of the MnO anode materials.

Considering the advantages of MnO-based hybrids and the relatively complex fabrication procedure of above studies, in this work, we demonstrate a simple, facile strategy to hybridize nanosized MnO with nitrogen-doped carbon (abbreviated as MnO/C−N). It is worth mentioning that in this MnO/C−N hybrid, MnO nanoparticles chemically combine with N-doped C by Mn−N bonding, not common compositing. Electrochemical measurements indicate that the MnO/C−N hybrid exhibits perfect lithium storage performance. It can display a specific capacity up to 1699 mAh g^{-1} at high current density of 0.5 A g^{-1} after 170 discharge−charge cycles, which is higher than those of most of reports on MnO-based materials. The reason may be mainly originated from two aspects. On the one hand, the bond formed between MnO particles and N-doped carbon limits the agglomeration of Mn nanoparticles generated during lithiation and at the same time the small size MnO and carbon can alleviate the structural strain resulting from the volume change during Li^+ insertion and extraction, as well as provide short lithium-ion transportation path during charge/discharge cycling. On the other hand, the highly conducting N-doped carbon matrix could provide a continuous pathway for electron transport.

2. EXPERIMENTAL SECTION

Synthesis of MnO/C−N Hybrid. In a typical synthesis, ascorbic acid (2 mmol) and $Mn(OAc)_2{\cdot}4H_2O$ (1 mmol) were added in 50 mL of ethanol. A transparent solution was then obtained after stirring for 30 min. Subsequently, hydrazine hydrate (2 mL) was added dropwise into above solution. The resultant solution was transferred into Teflon-lined stainless steel autoclave (80 mL), which was kept at 120 °C for 24 h. After the autoclave was cooled down to room temperature, a precursor can be obtained. Finally, the precursor was annealed in Ar/H_2 mixing atmosphere ($Ar:H_2$ = 93%:7%, volume) at 600 °C for 3 h at a heating rate of 3 °C min^{-1}. For comparison, the MnO/C hybrid was obtained in the absence of hydrazine hydrate and pure MnO was prepared without the addition of hydrazine hydrate and ascorbic acid, in which other conditions were kept as those of the typical experiment.

Characterizations. The composition and purity of the obtained samples were characterized using powder X-ray diffraction (XRD) with Cu Kα (λ = 1.54178 Å) incident radiation (Shimadzu XRD-6000) The corresponded scanning range and step were recorded from 30 to 80° (2θ) and of 6° min^{-1}, respectively. The morphology of the resulting samples was investigated by a transmission electron microscopy (TEM) (H-8100, with the accelerating voltage of 200 kV). Field emission scanning electron microscopy (FE-SEM) and energy-dispersive spectroscopy (EDS) element mapping test of the sample were taken on a SEM unit (Hitachi S-4800). Raman spectra were collected on an Invia Raman spectrometer, using an excitation laser of 514.5 nm. The carbon content was determined by the combustion method using an elemental analyzer (Vario EI). X-ray photoelectron spectra (XPS) were used to characterize the surface composition of the sample by using an ESCALAB 250 spectrometer (Perkin-Elmer). The thermogravimetry (TG) analysis of the hybrid was performed from 25 to 700 °C in air with a heating rate of 20 °C min^{-1} using a DTG-60AH instrument.

Electrochemical Measurements. Electrochemical measurement was carried out at room temperature by using coin cells (CR2025) on LAND CT2001A with a cutoff voltage of 0.01−3.00 V versus Li^+/Li. For the anode preparation, active material, acetylene black and polyvinylidene fluoride (PVDF) binder with a weight ratio of 80:10:10 was mixed and ground in a mortar. N-methylpyrrolidone (NMP) was selected as the solvent to make slurry. The prepared slurry was uniformly pasted on the Cu foil. Then the typical electrode was placed in a vacuum oven at 120 °C for 24 h before assembled into coin cell in an argon-filled glovebox. Li foil was used as the counter electrode. 1 M $LiPF_6$ dissolved in an ethylene carbonate (EC)/dimethyl carbonate (DMC)/diethyl carbonate (DEC) mixture (1:1:1, in wt%) was used asthe nonaqueous electrolyte. The loading of the active materials was 0.45 mg cm^{-2}. Cyclic voltammetry (CV) curves were carried out on a CHI-760E electrochemical workstation at a scanning rate of 0.1 mV s^{-1}. The impendence spectra were recorded with amplitude of 5 mV over the frequency range from 100 kHz to 0.005 Hz. The specific capacity for the MnO/C−N is calculated according to the total weight including MnO and the N-doped carbon.

3. RESULTS AND DISCUSSION

The as-obtained product was first examined by power X-ray diffraction (XRD). As shown in Figure 1a, all the diffraction peaks can be readily assigned to a cubic phase of MnO (JCPDS Card: 07-0230). The main peaks at 2$\theta \approx$ 35.0, 40.6, 58.7, 70.3, and 73.8° can be indexed as (111), (200), (220), (311) and (222) reflections of cubic MnO. The crystalline size of the MnO particles is calculated to be 26.2 nm using the Scherrer formula based on the (200) peak. No other diffraction peaks corresponding to crystalline byproducts are detected. Raman spectroscopy further confirmed the existence of MnO and carbon as well as N-doping in this sample (Figure 1b). The peaks observed at 361.9 and 647.6 cm^{-1} can be ascribed to the Mn−O vibration according to the literatures.[15,19] and the one

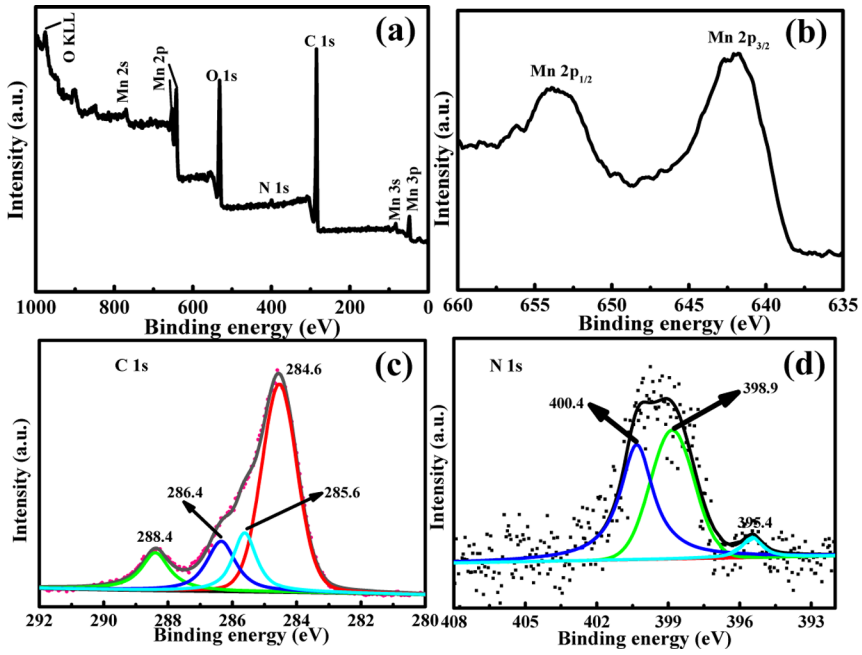

Figure 2. XPS spectra for the MnO/C–N bybrid: (a) the survey spectrum and the high resolution spectra for (b) Mn 2p, (c) C 1s, (d) N 1s.

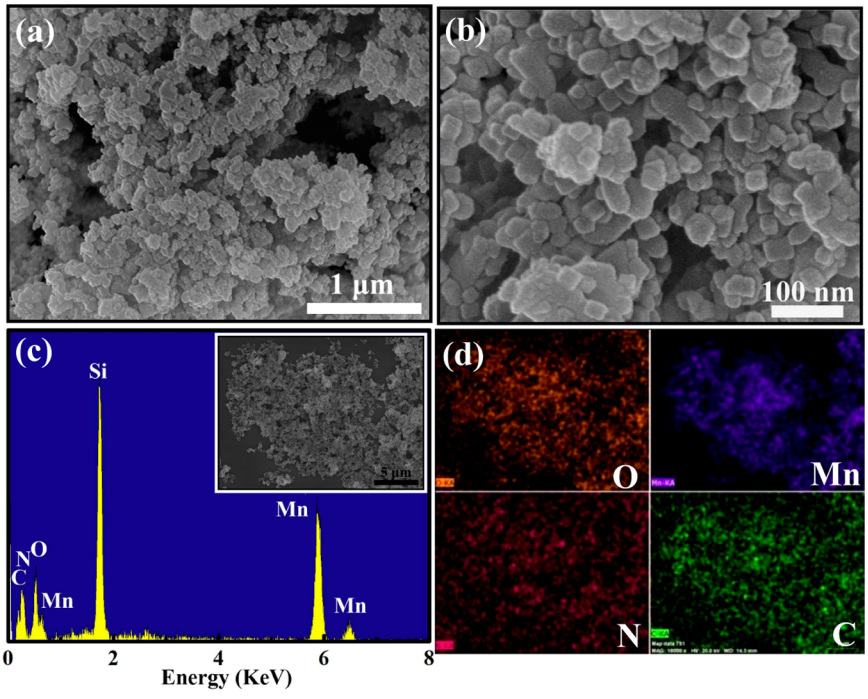

Figure 3. (a, b) Typical FE-SEM images of the MnO/C–N hybrid with different magnifications. (c) EDS spectrum of the MnO/C–N hybrid. (d) The element mapping images for O, Mn, N, and C, respectively. The inset in c is the selected SEM-image for element mapping test.

at 306.6 cm^{-1} may be related to Mn–N band.[21,22] The broad peaks at 1349.7 and 1584.7 cm^{-1} can be ascribed to the D and G bands of carbon, respectively.[23] Additionally, the high intensity of the D band suggests the existence of defects and non-graphitic carbon in the sample, which may be originated from the N-doping, and this kind of carbon has been well-demonstrated to possess more Li storage sites than graphitic carbon.[19] For comparison, the Raman spectra of MnO/C and MnO were also measured (Figure 1b). Obviously, MnO/C has similar Raman spectrum to MnO/C–N apart from the peaks centered at about 361.9 and 306.6 cm^{-1}, which indicates the formation of MnO/C and further confirms the bonding between N and Mn for MnO/C–N.[15,21,22] The Raman spectrum of MnO only displays one broad peak in the range of 494.3–696.5 cm^{-1}. According to the previous reports,[24−26] this result indicates the presence of higher valence of Mn in the MnO sample, which is probably due to the photochemically induced transformation during the test process. For MnO/C–N and MnO/C samples, the presence of carbon prevents MnO from oxidizing.

The carbon and nitrogen contents in the MnO/C–N hybrid evaluated by CHN element analysis is 23.9 and 6.5%,

dx.doi.org/10.1021/am405142p | ACS Appl. Mater. Interfaces 2014, 6, 2051−2058

respectively. In addition, the thermogravimetry (TG) analysis was also performed to further provide the contents of various components in this hybrid. As shown in Figure S1 in the Supporting Information, the first weight loss about 7.9% occurred between 25 and 200 °C, which can be due to the removal of adsorbed water, and the subsequent weight loss about 31.1% from 200 to 450 °C is related to oxidation of carbon including N, which is very close to the result from the CHN element analysis. The second weight increasing from 500 to 700 °C is due to the transformation of MnO to Mn_2O_3.[20,27] According to above results, we named this sample as MnO/C−N hybrid.

To further investigate the surface electronic state and the composition of the MnO/C−N hybrid, we performed X-ray photoelectron spectroscopy (XPS). The survey XPS spectrum (Figure 2a) confirmed the presence of Mn, O, C, and N elements. The high-resolution Mn 2p spectrum (Figure 2b) exhibits two signals at 641.8 eV for Mn $2p_{3/2}$ and 653.8 eV for Mn $2p_{1/2}$, respectively, demonstrating the characteristic of MnO, which agrees well with those of the previous literatures.[24,28] The XPS peak of C 1s (Figure 2c) can be fitted into four parts, including the peaks centered at 284.6, 285.6, 286.4, and 288.4 eV, corresponding to sp^3C−sp^3C, N−sp^2C, C−O−C, and C−O bonds, respectively. Similarly, the N 1s peak (Figure 2d) can be resolved into two peaks centered at 400.4 and 398.9 eV with a weak peak at 395.4 eV, which correspond to pyrrolic, pyridinic, and Mn−N bonds, respectively.[29,30] Both the Raman and XPS spectra confirmed the formation of Mn−N bond in this hybrid. The previous report has verified that the metal−N bond is probably indispensable for the high electrochemical performance.[4]

The as-prepared MnO/C−N hybrid was further examined by field-emission scanning microscopy (FE-SEM) and transmission electron microscopy (TEM). As shown in images a and b in Figure 3, the hybrid is composed of small particles with an average diameter of about 20−50 nm. In agreement with the result from XPS measurement, the energy-dispersive spectroscopy (EDS) spectrum also confirmed that this hybrid was composed of Mn, O, N, and C elements (Figure 3c). The surface-scanning element mapping clearly reveals that these elements are homogeneously distributed (Figure 3d).

The typical TEM images with different magnifications are shown in images a and b in Figure 4, disclosing that the hybrid consists of considerable MnO nanoparticles confined in the carbon matrix. Higher-magnification TEM image (Figure 4c) revealed that MnO particles were also coated with the carbon layer marked by yellow circle, which may make the MnO particles firmly confined in the carbon matrix and subsequently improve the electrochemical performance. Figure 4d shows the high-resolution TEM (HRTEM) image of the single MnO nanoparticles. The lattice fringe with an interplanar distance of 0.22 nm can be attributed to the (200) plane of MnO. The diffraction rings in Figure 4d (the inset) indicate the polycrystalline nature of the product.

The electrochemical performance of the MnO/C−N hybrid is investigated as anode materials in lithium ion batteries. Its electrochemical process is first studied by the cyclic voltammogram (CV) curves. Figure 5a shows representative cyclic voltammetry (CV) curves of the initial five cycles at a scan rate of 0.1 mV s^{-1} in the range of 0.01−3.00 V, which accords with the previous reports.[14,15,20] In the first catholic sweep, the sharp reduction peak at 0.16 V refers to the transformation from Mn^{2+} to Mn^0 and the formation of solid electrolyte interface

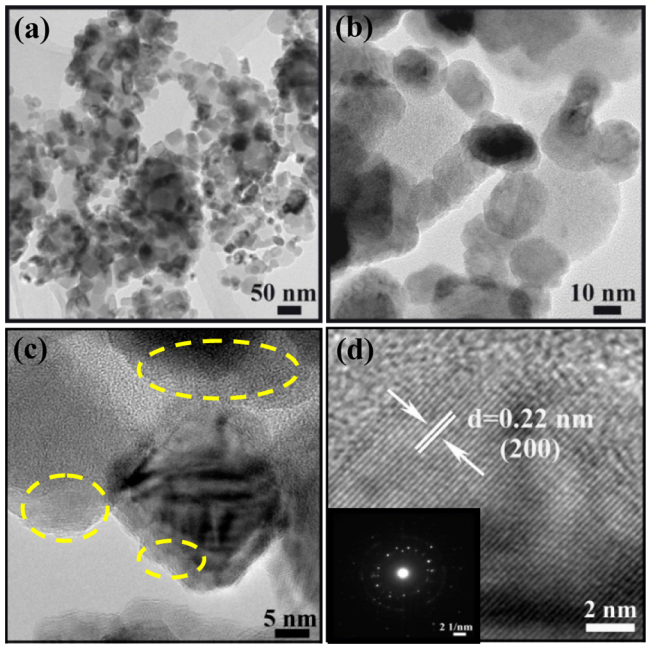

Figure 4. (a−c) TEM images of the MnO/C−N hybrid. (d) HRTEM image of the MnO/C−N hybrid, the inset one is the corresponding SAED pattern.

(SEI) layers. From the second cycle, the reduction peak shifts to 0.31 V, indicating an irreversible phase transformation arising from the formation of Mn and Li_2O.[19,20,31−34] The observed anode peak centered at 1.38 V could be ascribed to the oxidation reaction of Mn^0 to Mn^{2+}. These processes can be expressed by the following reactions

$$MnO + 2Li^+ + 2e^- \rightarrow Mn + Li_2O \quad (1)$$

$$Mn + Li_2O \rightarrow MnO + 2Li^+ + 2e^- \quad (2)$$

The CV profiles after the first cycle are overlapped well, indicating high reversibility and good stability of the MnO/C−N hybrid.

Figure 5b shows the discharge−charge voltage profiles cycled at 0.5 A g^{-1} within a cutoff voltage window of 0.01−3.00 V vs. Li^+/Li. During the initial discharge process, a long voltage plateau at about 0.30 V can be clearly observed, which is related to the reduction of Mn^{2+} to Mn, whereas for the first charge process, the observed slope between 1.2 and 2.0 V is associated with the oxidation of Mn^0 to Mn^{2+}, which is typical characteristic of voltage trends for the MnO electrode.[33,34] From the second cycle, the discharge plateau has shifted to about 0.45 V, which may result from the enhanced kinetics and also indicates the irreversible formation of metal nanoparticles and Li_2O.[33,35] Moreover, it can also be seen from Figure 5b that the first discharge and charge specific capacities are 1717.5 and 1217.0 mAh g^{-1}, respectively, indicating an initial Coulombic efficiency of 70.9%, which is common for the reported transition metal oxide anodes.[27] And the capacity loss in the first cycle is mainly ascribed to the formation of solid electrolyte interface (SEI) films on the surface of the electrode, similar to most of reports on LIBs.[1−6,31] Though there is a large irreversible capacity loss in the first cycle, the specific capacity was still up to 1231.1 mAh g^{-1} in the second cycle. Interestingly, after about 70 cycles, the charge slop at about 1.5−2.5 V gradually appears in the correspondingdischarge−

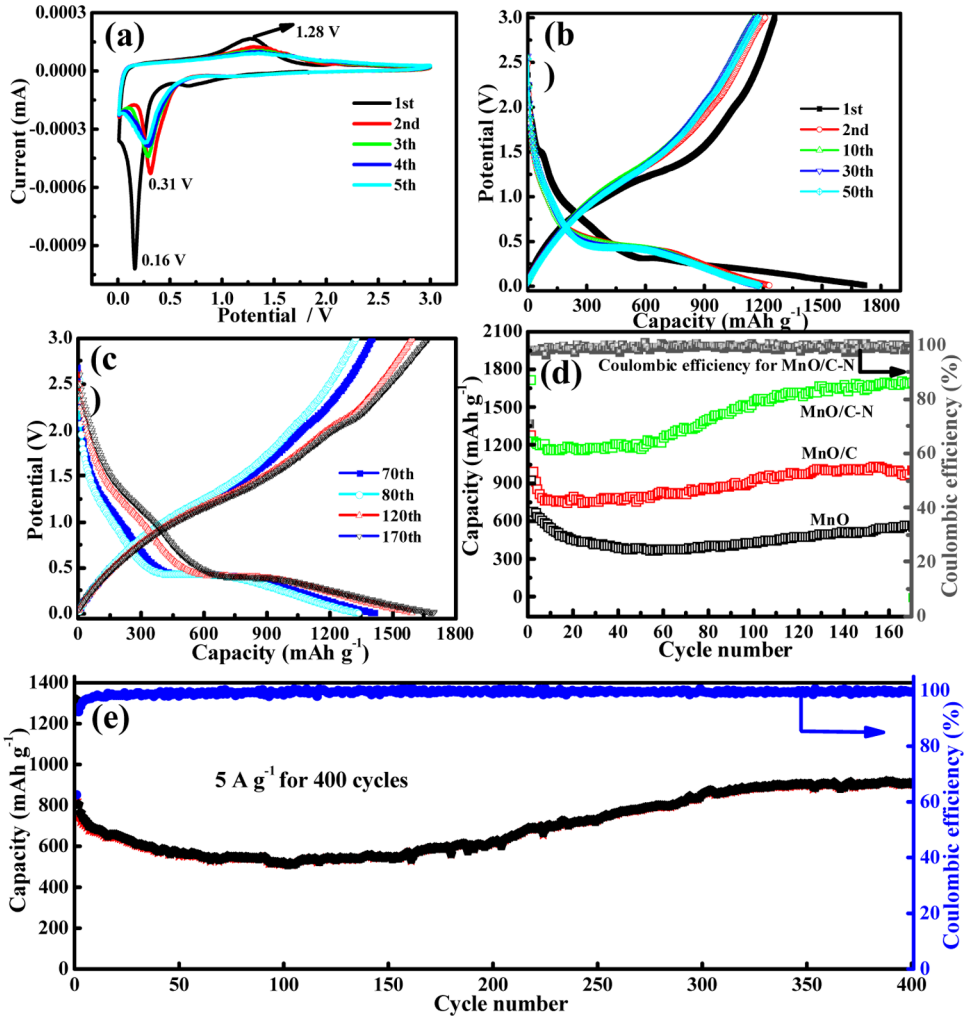

Figure 5. (a) CV curves of the MnO/C−N hybrid for the first five cycles. (b, c) Discharge and charge profiles of the MnO/C−N hybrid at 0.5 A g^{-1} between 0.01 and 3.00 V for different cycles. (d) Cycling performance of MnO/C−N, MnO/C and pure MnO at 0.5 A g^{-1}, and the corresponded Columbic efficiency of the MnO/C−N hybrid. (e) Cycle performance of the MnO/C−N at 5 A g^{-1} for 400 cycles and the related Coulombic efficiency.

charge profiles, which is similar to the previous reports and is considered to be related to the oxidation of Mn^{2+} to a higher state (Figure 5c).[14−16]

Figure 5d displays the cycling performance the MnO/C−N hybrid electrodes at 0.5 A g^{-1} in the range of 0.01−3.00 V vs. Li^+/Li. For comparison, those of MnO/C and MnO are also provided at the same tested conditions (see Figure S2 in the Supporting Information). It can be clearly observed that the MnO/C−N hybrid shows the most excellent cycling performance compared to the MnO/C and the pure MnO. The Coulombic efficiency of the MnO/C−N steadily reaches above 99.0% with the cycling number increasing. More importantly, the reversible capacity after 170 cycles is as high as 1699 mAh g^{-1}, which is more than twice the theoretical capacity of MnO (755 mAh g^{-1}) and over four times higher than the theoretical capacity of graphite (372 mAh g^{-1}). This phenomenon is also common in other transition metal oxides.[16,20] According to the previous reports, the reason may be attributed to the formation of polymeric gel-like film due to the kinetically active electrolyte degradation during conversion process and the defects formed by the N-doping,[36,37] which enhance the lithium storage capacity of MnO. In contrast, MnO/C and pure MnO samples display discharge capacities of 1003.5 and 572.6 mAh g^{-1} after 170 cycles, respectively, both of which are largely lower than that of MnO/C−N. This result indicates that the C and N existed in the MnO/C−N hybrid play a key role in the significant enhancement of the capacity. According to the literatures, N-doping generally leads to more defects, while in turn these defects possess large adsorption energies of the Li ions and low energy barrier for the lithium penetrating these defects, which may partially ensure the active materials' capability for lithium storage.[37−40] Therefore, it can be concluded that it is the synergy effect of C hybridization and N-doping that greatly enhance the whole performance of the MnO-based electrode. Additionally, even at a high current density of 5 A g^{-1}, the MnO/C−N still exhibits superior lithium storage performance, as displayed in Figure 5e.

A satisfactory reversible capacity of 907.8 mAh g^{-1} after 400 cycles can be retained and the Coulombic efficiency after initial cycle increases to above 99%, indicating the high capability and excellent cyclability. To the best of our knowledge, the above lithium storage performance of the MnO/C−N hybrid is much better than those of the reported MnO-based materials (Table 1).

Besides, it can be found that for the MnO/C−N hybrid the capacity gradually increases from the sixtieth cycle and finally

dx.doi.org/10.1021/am405142p | ACS Appl. Mater. Interfaces 2014, 6, 2051−2058

Table 1. Comparison of the Capacity of Present Work with Reported MnO-Based Materials[a]

samples	current density (mA g^{-1})	cycle number	capacity (mAh g^{-1})	ref
MnO@C nanoplates	200	30	563	13
mesoporous MnO/C networks	200 (1500)	200 (200)	1224 (731)	15
MnO/graphene hybrid	200 (2000)	150 (400)	2014 (843)	16
N-doped MnO/graphene	100	90	772	17
carbon-encapsulated MnO/N−C	1000	700	1268	18
hollow porous MnO/C spheres	100	50	702	23
hierarchical nanostructured MnO	98.3	200	782	27
MnO@C	100	80	800	32
MnO/C core−shell rods	200	40	about 600	33
MnO/Co	100	20	<500	41
MnO/Co nanocomposites	100	20	<400	42
MnO@carbon core−shell nanowires	500	200	801	43
porous C−MnO disks	100	140	1044	44
MnO/C−N hybrid	500 (5000)	170 (400)	1699 (908)	this work

[a]The current density values in parentheses in the second column correspond to the cycles in parentheses in the third column and the capacity values in parentheses in the fourth column.

stabilizes, which has also been observed in other MnO-based electrodes.[15,45,46] The gradual increase in capacity with cycling is probably due to the improved conversion-reaction kinetics resulting from the formed defects in the electrodes during discharge/charge processes, resulting in the oxidation of Mn^{2+} to a higher oxidation state. This process is confirmed by the XPS measurement of the MnO/C−N electrode after 400 cycles at 5 A g^{-1}. As displayed in Figure S4 in the Supporting Information, two weak peaks in the XPS spectrum of Mn 2p can be detected, the binding energies of which have shifted to higher value compared to those of the uncycled one, indicating the oxidation of Mn^{2+}.[18,38−40,46,47]

Furthermore, it is worth noting that the MnO/C−N hybrid presents wonderful rate capability. The rate performance of the three samples was tested by increasing the current density stepwise from 0.1 to 5 A g^{-1} and subsequently coming back to 0.1 A g^{-1}. As displayed in Figure 6. It can be observed that the MnO/C−N hybrid exhibits significantly enhanced rate performance compared to other two samples. Even after a high rate of 5 A g^{-1}, the capacity could be recovered to the value close to the initial one when the rate went back to 0.1 A g^{-1}, implying the good reversibility of this materials. The excellent rate performance of the MnO/C−N hybrid should closely associated with its high conductivity, which was verified by the electrochemical impedance spectrum (EIS) measurements after 170 cycles at 0.5 A g^{-1}. As shown in Figure S4 in the Supporting Information, the Nyquist plots all consist of two parts including a depressed semicircle and a straight line in the region of high-middle and low frequency, respectively.. The diameter of the semicircle for the MnO/C−N hybrid is obviously smaller than those of the other two samples (MnO/C and MnO), providing the fact that the MnO/C−N hybrid has lower contact and charge-transfer impedances.[48,49] This result shows that the co-existence of C and N plays a prominent role in increasing the conductivity of MnO.

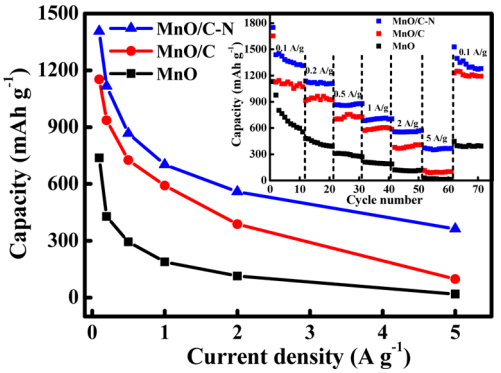

Figure 6. Rate performance comparison of the samples at a current density from 0.1 to 5 A g^{-1}. The inset one is the corresponded rate capability and cycle performance at varied current densities.

To provide further insight into the excellent performance of the MnO/C−N hybrid, we tested the morphology of the MnO/C−N electrode after 170 cycles at discharge state at 0.5 A g^{-1}. TEM examination finds that the MnO/C−N still maintains its original morphology and no discernible aggregation is observed (Figure 7a). Moreover, the size of the MnO/C−N particles almost does not change compared to that before cycling. The excellent structural stability could be ascribed to the confinement effects of the conductive carbon matrix and the carbon layer around nanoparticles, which could accommodate the volume change during cycling. Meanwhile, the HRTEM image (the interplane distance is 0.21 nm) discloses the formation of Mn particles during the lithiation process (Figure 7b). However, after 400 discharge−charge cycles at a higher rate (5 A g^{-1}), the original particles have broken into smaller grains (less than 10 nm) with better distribution (Figure 7c). As demonstrated by previous studies, the smaller size of active materials will partially alleviate the volume change and significantly reduce the Li^+ transport path, which benefit to the high electrochemical performance.[17,18]

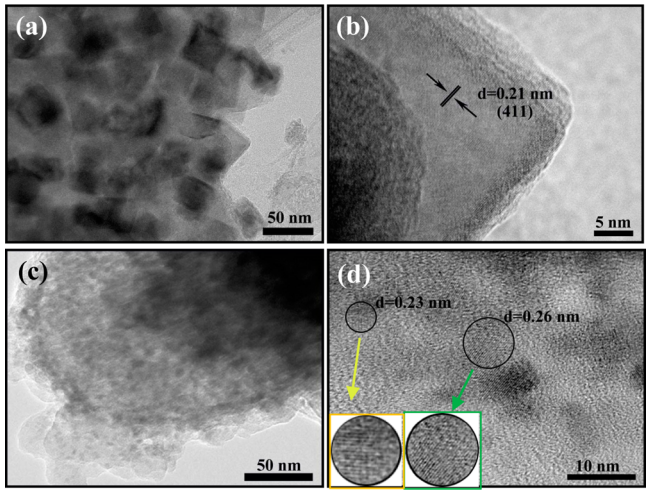

Figure 7. TEM and HRTEM images of the MnO/C−N hybrid after cycling at different conditions: (a, b) after 170 cycles at discharged state; (c, d) after 400 cycles at the charged state.

Besides, the formation of higher oxidation state of MnO_2 (the interplanar distance is 0.23 nm) in the delithiation process was also detected (Figure 7d), probably originating from the formed defects in the electrodes during the electrochemical process, which improve the conversion-reaction kinetics of the electrode.

According to above results, we believe that the high capacity, superior cyclability, and excellent rate capability of the as-obtained MnO/C−N hybrid result from its unique hybrid structure and the N-doping as well as the chemical bonding of MnO and N-doped C (Figure 8). During the electrochemical

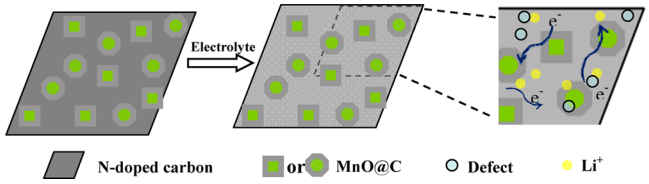

Figure 8. Schematic process of the diffusion of electrolyte, and the transportation of electrons and lithium ions in the MnO/C−N hybrid.

process, on the one hand, the highly conducting N-doped carbon has good conductivity and elasticity, which not only provide a continuous pathway for electron transport, but also could buffer the volume change and avoid the aggregation of the MnO nanoparticles; on the other hand, the N-doping induces more defects, which may provide additional Li insertion sites and enhance the lithium storage of the active materials. Additionally, the small size of the MnO nanoparticles may be able to alleviate the strain resulting from the particle volume expansion/contraction during the cycling process to some extent. Besides, the interaction between Mn and N also partially contributes to the lithium storage performance.

4. CONCLUSION

In summary, we have reported a facile strategy to fabricate MnO/C−N hybrid using a hydrothermal method followed by calcining treatment. The resultant hybrid displays excellent lithium storage performance when used as anode materials in LIBs. A reversible capacity of 1699 mAh g^{-1} could be obtained at 0.5 A g^{-1}, and even at the high current density up to 5 A g^{-1}, 907.8 mAh g^{-1} of the capacity can be retained. Additionally, the current synthesis strategy is low cost, effective, and it may be used to prepare other transition metal oxide nanomaterials, which have wide applications in catalysis and electrochemical areas.

■ ASSOCIATED CONTENT

Supporting Information

TG of the precursor for the MnO/C−N hybrid, SEM images of the control samples, XRD patterns of the control samples, XPS spectrum of the Mn 2p after 400 discharge/charge cycles, and the Nyquist plots for all samples. This material is available free of charge via the Internet at http://pubs.acs.org/.

■ AUTHOR INFORMATION

Corresponding Author

*Fax: +86-10-68918572. Tel: +86-10-68918468. E-mail: caomh@bit.edu.cn.

Notes

The authors declare no competing financial interest.

■ ACKNOWLEDGMENTS

This work was supported by the National Natural Science Foundation of China (21271023, 91022006, and 20973023) and the 111 Project (B07012)

■ REFERENCES

(1) Wu, H. B.; Chen, J. S.; Hng, H. H.; Lou, X. W. *Nanoscale* **2012**, *4*, 2526−2542.
(2) Xue, D. J.; Xin, S.; Yan, Y.; Jiang, K. C.; Yin, Y. X.; Guo, Y. G.; Wan, L. J. *J. Am. Chem. Soc.* **2012**, *134*, 2512−2515.
(3) Zhou, L.; Zhao, D. Y.; Lou, X. W. *Angew. Chem.* **2012**, *124*, 243−245.
(4) Zhou, X. S.; Wan, L. J.; Guo, Y. G. *Adv. Mater.* **2013**, *25*, 2152−2157.
(5) Jang, B.; Park, M.; Chae, O. B.; Park, S.; Kim, Y.; Oh, S. M.; Piao, Y.; Hyeon, T. *J. Am. Soc. Chem.* **2012**, *134*, 15010−15015.
(6) Nam, I.; Kim, N. D.; Kim, G. P.; Park, J.; Yi, J. *J. Power Sources* **2013**, *244*, 56−62.
(7) Xiao, Y.; Hu, C. W.; Cao, M. H. *J. Power Sources* **2014**, *247*, 49−56.
(8) Wen, W.; Wu, J. M.; Cao, M. H. *Nano Energy* **2013**, *2*, 1383−1390.
(9) Qu, J.; Yin, Y. X.; Wang, Y. Q.; Yan, Y.; Guo, Y. G.; Song, W. G. *ACS Appl. Mater. Interfaces* **2013**, *5*, 3932−3936.
(10) Wei, W.; Yang, S. B.; Zhou, H. X.; Lieberwirth, I.; Feng, X. L.; Müllen, K. *Adv. Mater.* **2013**, *25*, 2909−2914.
(11) Sun, Y. M.; Hu, X. L.; Luo, W.; Huang, Y. H. *J. Mater. Chem.* **2012**, *22*, 425−431.
(12) Cheng, F. Y.; Shen, J. A.; Peng, B.; Pan, Y. D.; Tao, Z. L.; Chen, J. *Nat. Chem.* **2011**, *3*, 79−84.
(13) Zhang, X.; Xing, Z.; Wang, L. L.; Zhu, Y. C.; Li, Q. W.; Liang, J. W.; Yu, Y.; Huang, T.; Tang, K. B.; Qian, Y. T.; Shen, X. Y. *J. Mater. Chem.* **2012**, *22*, 17864−17869.
(14) Fang, X. P.; Lu, X.; Guo, X. W.; Mao, Y.; Hu, Y. S.; Wang, J. Z.; Wang, Z. X.; Wu, F.; Liu, H. K.; Chen, L. Q. *Electrochem. Commun.* **2010**, *12*, 1520−1523.
(15) Luo, W.; Hu, X. L.; Sun, Y. M.; Huang, Y. H. *ACS Appl. Mater. Interfaces* **2013**, *5*, 1997−2003.
(16) Sun, Y. M.; Hu, X. L.; Luo, W.; Xia, F. F.; Huang, Y. H. *Adv. Funct. Mater.* **2013**, *23*, 2436−2444.
(17) Ren, Y.; Armstrong, A. R.; Jiao, F.; Bruce, P. G. *J. Am. Chem. Soc.* **2010**, *132*, 996−1004.
(18) Wang, Y.; Zhang, H. J.; Lu, L.; Stubbs, L. P.; Wong, C. C.; Lin, J. *ACS Nano* **2010**, *4*, 4753−4761.
(19) Zhang, K. J.; Han, P. X.; Gu, L.; Zhang, L. X.; Liu, Z. H.; Kong, Q. S.; Zhang, C. J.; Dong, S. M.; Zhang, Z. Y.; Yao, J. H.; Xu, H. X.; Cui, G. L.; Chen, L. Q. *ACS Appl. Mater. Interfaces* **2012**, *4*, 658−664.
(20) Chen, W. M.; Qie, L.; Shen, Y.; Sun, Y. M.; Yuan, L. X.; Hu, X. L.; Zhang, W. X.; Huang, Y. H. *Nano Energy* **2013**, *2*, 412−418.
(21) Bernarda, M.; Deneuville, A.; Thomasb, O.; Gergaudb, P.; Sandstrom, P.; Birch, J. *Thin Solid Films* **2000**, *380*, 252−255.
(22) Yang, X. L.; Wu, J. J.; Chen, Z. T.; Pan, Y. B.; Zhang, Y.; Yang, Z. J.; Yu, T. J.; Zhang, G. Y. *Solid State Commun.* **2007**, *143*, 236−239.
(23) Xiao, Y.; Hu, C. W.; Cao, M. H. *Chem.—Asian. J.* **2014**, *9*, 351−356.
(24) Xia, Y.; Xiao, Z.; Dou, X.; Huang, H.; Lu, X. H.; Yan, R. J.; Gan, Y. P.; Zhu, W. J.; Tu, J. P.; Zhang, W. K.; Tao, X. Y. *ACS Nano* **2013**, *7*, 7083−7092.
(25) Mai, Y. J.; Zhang, D.; Qiao, Y. Q.; Gu, C. D.; Wang, X. L.; Tu, J. P. *J. Power Sources* **2012**, *216*, 201−207.
(26) Buciuman, F.; Patcas, F.; Craciun, R.; Zahn, D. R. T. *Phys. Chem. Chem. Phys.* **1999**, *1*, 185−190.
(27) Xu, G. L.; Xu, Y. F.; Fang, J. C.; Fu, F.; Sun, H.; Huang, L.; Yang, S.; Sun, S. G. *ACS Appl. Mater. Interfaces* **2013**, *5*, 6316−6323.
(28) Li, X. N.; Zhu, Y. C.; Zhang, X.; Liang, J. W.; Qian, Y. T. *RSC Adv.* **2013**, *3*, 10001−10006.
(29) Ming, H.; Li, X. W.; Su, L. L.; Liu, M. M.; Jin, L. L.; Bu, L. J.; Kang, Z. H.; Zheng, J. W. *RSC Adv.* **2013**, *3*, 3836−3839.

(30) Jiao, W.; Li, N.; Wang, L. Z.; Wen, L.; Li, F.; Liu, G.; Cheng, H. M. *Chem. Commun.* **2013**, *49*, 3461−3463.
(31) Hu, C. G.; Xiao, Y.; Zhao, Y.; Chen, N.; Zhang, Z. P.; Cao, M. H.; Qu, L. T. *Nanoscale* **2013**, *5*, 2726−2733.
(32) Wang, T. Y.; Peng, Z.; Wang, Y. H.; Tang, J.; Zheng, G. F. *Sci. Rep.* **2013**, *3*, 2693−2701.
(33) Sun, B.; Chen, Z.; Kim, H. S.; Ahn, H.; Wang, G. *J. Power Sources* **2011**, *196*, 3346−3349.
(34) Liu, J.; Pan, Q. M. *Electrochem. Solid-State Lett.* **2010**, *13*, A139−A142.
(35) Liu, Y. M.; Zhao, X. Y.; Li, F.; Xia, D. G. *Electrochim. Acta* **2011**, *56*, 6448−6452.
(36) Grugeon, S.; Laruelle, S.; Dupont, L.; Tarascon, J. M. *Solid State Sci.* **2003**, *5*, 895−904.
(37) Mao, Y.; Duan, H.; Xu, B.; Zhang, L.; Hu, Y. S.; Zhao, C. C.; Wang, Z. X.; Chen, L. Q.; Yang, Y. S. *Energy Environ. Sci.* **2012**, *5*, 7950−7955.
(38) Wang, H. B.; Zhang, C. J.; Liu, Z. H.; Wang, L.; Han, P. X.; Xu, H. X.; Zhang, K. J.; Dong, S. M.; Yao, J. H.; Cui, G. L. *J. Mater. Chem.* **2011**, *21*, 5430−5434.
(39) Zhou, Z.; Gao, X. P.; Yan, J.; Song, D. Y.; Morinaga, M. *Carbon* **2004**, *42*, 2677−2682.
(40) Li, Y. F.; Zhou, Z.; Wang, L. B. *J. Chem. Phys.* **2008**, *129*, 104703−104707.
(41) Kokubu, T. K.; Oaki, Y. Y.; Hosono, E. J.; Zhou, H. S.; Imai, H. K. *Adv. Funct. Mater.* **2011**, *21*, 3673−3680.
(42) Dang, F.; Oaki, Y. Y.; Kokubu, T. K.; Hosono, E. J.; Zhou, H. S.; Imai, H. K. *Chem.—Asian J.* **2013**, *8*, 760−764.
(43) Li, X. W.; Xiong, S. L.; Li, J. F.; Liang, X.; Wang, J. Z.; Bai, J.; Qian, Y. T. *Chem. -Eur. J.* **2013**, *19*, 11310−11319.
(44) Sun, Y. M.; Hu, X. L.; Luo, W.; Huang, Y. H. *J. Mater. Chem.* **2012**, *22*, 19190−19195.
(45) Xu, G. L.; Xu, Y. F.; Sun, H.; Fu, F.; Zheng, X. M.; Huang, L.; Li, J. T.; Yang, S. H.; Sun, S. G. *Chem. Commun.* **2012**, *48*, 8502−8504.
(46) Guo, J. C.; Liu, Q.; Wang, C. S.; Zachariah, M. R. *Adv. Funct. Mater.* **2012**, *22*, 803−808.
(47) Xia, H.; Lai, M.; Lu, L. *J. Mater. Chem.* **2010**, *20*, 6896−6902.
(48) Yang, S.; Feng, X.; Zhi, L.; Cao, Q.; Maier, J.; Mullen, K. *Adv. Mater.* **2010**, *22*, 838−842.
(49) Xiao, Y.; Hu, C. W.; Cao, M. H. *Chem.—Eur. J.* **2013**, *19*, 10193−10200.